COLORADO SCHOOL OF MINES - FINAL REPORT

Measurement of the Effect of Magnetism on Hydrogen Cracking Susceptibility of Pipeline Steels – Joint Industry Project

Contract Number: **0106CT39654**

Submitted to:

DOI - MINERAL MANAGEMENT SERVICES

DOT - PIPELINE AND HAZARDOUS MATERIALS SAFETY ADMINISTRATION

Attn: **MICHAEL ELSE**

US DEPARTMENT OF THE INTERIOR

Technology Assessment & Research Branch

381 Elden St., MS 4700

Herndon, VA 20170-4817

Attn: **KIMBERLY LUKE**

U.S. DEPARTMENT OF THE INTERIOR

Mineral Management Service

381 Elden St., MS 2500

Herndon, VA 20170-4817

Attn: **ROBERT SMITH**

US DEPARTMENT OF TRANSPORTATION - PHMSA

Office of Pipeline Safety

400 7th St., SW

Washington, D.C. 20590

Submitted by:

Prof. David L. Olson

Prof. Brajendra Mishra

J. A. Roubidoux

Measurement of the Effect of Magnetism on Hydrogen Cracking Susceptibility of Pipeline Steels – Joint Industry Project

SCOPE

The behavior of thick high-strength pipeline steels was assessed under simulated field conditions including assessment of (1) steel strength, (2) stresses due to cold work, surface damage, and fluid pressure, (3) hydrogen activity related to cathodic protection, soil conditions, and fluids carried in the pipe, (4) temperature, and (5) remanent magnetism in steels after pigging with magnetic inline inspection tools. The values for (1)-(5) will be varied to simulate field conditions. This project aims to measure electrochemical corrosion and hydrogen induced cracking susceptibility of pipeline steel under simulated conditions in a quantitative manner.

OBJECTIVES

A Joint Industry Project (JIP) has been established to assess the change in hydrogen damage susceptibility due to magnetization under simulated field conditions of magnetic flux leakage inline inspection. Industrial and federal members participated through in-kind and financial assistance. Simulation of field parameters, with the assistance of the JIP partners, was used in the testing, characterization, and modeling being performed at the Colorado School of Mines for this JIP.

The project objectives include:

- Determination of field conditions for remnant magnetization, hydrogen content in pipes (surface & bulk), temperature and stress profile (dents and bulk) by (i) literature review of pigging operation and data, (ii) field data analysis and (iii) visit of field pigging operations

- Measurement of the amount of hydrogen absorbed in electrolytically-charged pipeline steel samples by LECO Hydrogen Analyzer.

- Measurement of temperature effect on hydrogen absorption. Steel samples will be tested in –30 to + 50^{o}C temperature regime (3 temperatures).

- Characterization of hydrogen induced cracking, anodic pitting and stress corrosion cracking in all samples as a function of:
    - Steel grade (strength)
    - Magnetic field
    - Temperature

- Correlation with hydrogen content, magnetic field and hydrogen cracking susceptibility.

1.0 INTRODUCTION

Magnetocorrosion is the altered corrosion behavior, including changes in hydrogen ingress, experienced in the presence of a magnetic field. The combination of magnetic and electric fields alters the magnetocorrosion behavior of pipeline steels, including the measured hydrogen content, pitting, and cracking. Laboratory electrochemical hydrogen charging measurements in the presence of a magnetic field indicate a significant increase in magnetocorrosion (including hydrogen content, pitting, and cracking) compared to unmagnetized charging.

This research evaluated the thermodynamics and kinetics of corrosion, and evaluated the correlation of magnetocorrosion to microstructure, mechanical properties, and magnetic properties. Proposed thermodynamic models including the effects of spin alignment, magnetostriction, and solute-strain have been developed. A possible kinetic model for enhanced hydrogen pickup and corrosion based on surface effects associated with the Gouy-Chapman Layer and the Helmholtz Double layer is examined. Disturbance of these layers acts to limit hydrogen transport from the environment into the steel and the transport of anodic product ions to the surface. The combination of large magnetic fields and cathodic protection currents returning in the pipe simultaneously may disturb these surface layers. Alteration of these layers may result in hydrogen super-saturation of the steel by directly altering the system kinetics. Each of these effects on the hydrogen content in magnetized steel is mechanistically described.

Magnetic fields, in combination with electric currents, have a significant effect on laboratory measurements of pipeline steel corrosion, seriously increasing measured corrosion behavior, including hydrogen content and hydrogen-induced cracking and pitting. Specimens of pipeline steel were electrochemically charged under a simulated cathodic protection voltage, with and without an applied magnetic field of maximum strength of approximately 1.0 and 0.6 Tesla. In preliminary work it was observed the application of cold work to the specimens through bending further increased the measured hydrogen content and corrosion behavior [Sanchez et al, 2005]. Thermodynamic and kinetic modeling of the influence of magnetic and electric fields on pipeline steel corrosion were previously described [Jackson, 2006].

Surveys of pipeline hydrogen content have indicated a sixfold increase in hydrogen content after one to two years of operation and greater than tenfold increase after more than ten years in operation [Mazel, 1995]. Stress corrosion cracking has been related to failures in coated and uncoated pipelines, both with and without cathodic protection. Between 1965 and 1986 in the United States, more than 250 failures were identified as stress corrosion cracking. The majority of the pipeline infrastructure in the United States is over forty years old, and some operating lines are over seventy years old. Many of these lines were designed for an expected operational lifetimes of 25-30 years. A review of the statistics of pipeline fractures found that a diameter increase from 820 to 1020 mm drastically increased the length of pipeline ruptures from 29 to 50 meters and decreased the average operating time of pipelines from 21 to 13.7 years [Polyakov and Kharionovsky, 1996]. The pipeline industry is increasingly using stronger steels, thinner wall dimensions, and larger pipe diameters, along with increasingly negative potentials being utilized for cathodic protection. These changes are likely to significantly increase the number of stress-corrosion and hydrogen-assisted failures [Shipilov, 2007].

Sources of magnetic fields (such as non-destructive testing, magnetic clamps and lifts, and welding) are numerous in pipelines. Likewise, electric fields are often present due to cathodic protection currents, which are constantly utilized in many pipelines to decrease the corrosion rate. Furthermore, hydrogen-enhanced fatigue cracking is responsible for many failures and is a significant concern for steel pipelines.

The apparent hydrogen solubility of pipeline steels is dependent upon a variety of factors including the presence of non-metallic inclusions and amount of cold work, which increase the number of hydrogen trapping sites [Maroef et al, 2002]. Pipelines have many high-stress regions, such as weldments, grain boundaries, voids, crack tips, and hoop stresses, the last of which is the largest. Hydrogen-induced cracks, fatigue cracks, cracks in the weld HAZ, and stress corrosion cracks are the most common types of cracking in pipelines. Other factors may change the hydrogen absorption rate and saturation concentration, such as exposure to acidic environments or disturbance of the Helmholtz Double Layer and/or Gouy-Chapman Layer.

2.0 EXPERIMENTAL PROCEDURES AND MATERIALS

The experimental procedures and materials are described for each task in the current period. The X52, X65, X70, and X80 grade steels were obtained from NIST and Xcel and analyzed for composition, metallography, and mechanical properties, and the X100 steel has now been received at NIST and is awaiting cutting and delivery from NIST-Boulder.

2.1 Metallurgical Evaluation of Pipeline Steel

The paradigm of composition, microstructure, and properties is being utilized to assess the metallurgical state and mechanical performance of the pipeline steels, and to correlate the corrosion behavior to these materials characteristics.

2.1.1 Composition

Low-carbon pipeline steel samples following the API 5L specifications for grades X52 and X65 are currently being used in the investigation and grade X100 will be characterized and included in the experimental matrices for this JIP upon delivery from NIST-Boulder. Preliminary measurements with atomic absorption spectroscopy have been performed on X52, X70, and X80 grade steels and complete characterization by optical emission spectroscopy have been performed on X52, X65 grade pipeline steels.

2.1.2 Metallography

The metallographic preparation included grinding on silicon carbide grinding paper to 600 grit and polishing to 6 micron with diamond polish. The samples were etched, when needed, and examined by optical microscopy.

2.1.3 Mechanical Properties Assessment

Tensile testing specimens of standard size were produced from the large-diameter pipeline steel specimens in both the longitudinal and radial directions (when possible as limited by the pipeline section diameter and thickness), using three specimens each from the X52 longitudinal, X65 longitudinal, and X65 radial orientations. The typical API 5L tensile testing specifications were used and tests were performed on the MST Alliance model RT/100 tensile testing system, as shown in Figure 1 below. The RT/100 tensile tester has a nominal capacity of 100,000 Newtons

(22,500 lbs). Microhardness testing was used to assess the material hardness on the microscopic scale. Microhardness test results may be converted through commonly available tables to other hardness scales, such as the Rockwell scales, or to an approximate yield strength or ultimate tensile strength units (psi).

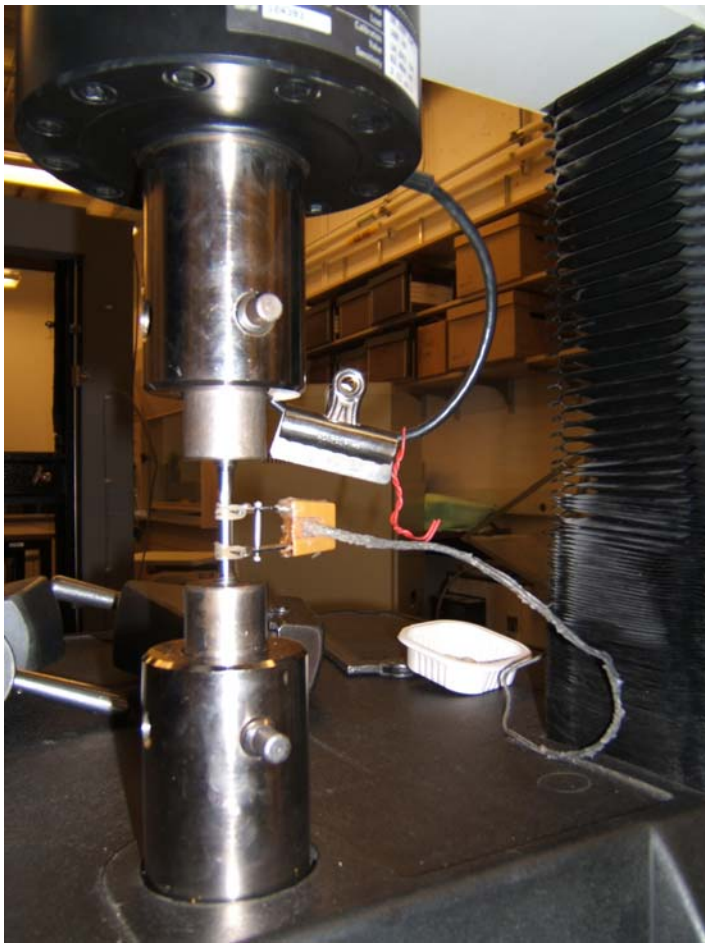

Figure 1 – Tensile property measurement setup in the Alliance Model RT/100 tensile tester.

3.0 RESULTS AND DISCUSSION

The results and work-in-progress for each task in the current period of work is presented. Discussion of the results and ongoing work includes the metallurgical assessment, quantitative electrochemical hydrogen-charging cell, electrochemical impedance, magnetic properties measurement, and AC corrosion experiments.

3.1 Metallurgical Evaluation of Pipeline Steel Specimens

The correlation of composition, microstructure, and mechanical properties with magnetocorrosion and magnetic properties will allow more accurate determination of the important parameters in magnetocorrosion.

3.1.1 Composition

The steel samples used for the laboratory tests were low-carbon steel, produced according to API 5L Grade X52, X65, X70, and X80 specifications. The tables below give composition

measurements with the associated API 5L standards for each steel strength. Table 2 shows the preliminary composition assessment as performed by atomic absorption spectrometry for the X52 grade steel tested in this study. Table 2a gives a more thorough analysis of the major compositional elements using optical emission spectroscopy (OES) and Leco interstitial analysis. Table 3 gives the optical emission spectroscopy (OES) and Leco interstitial analysis for X65 grade steel, Table 4 and 5 give the atomic absorption spectrometry (AAS) measurements and the API specification for X70 and X80 (respectively) grade pipeline steels. The tests are performed according to API Spec5L testing procedure that refers to the requirements of the ASTM A370 specification.

Table 2. Preliminary atomic absorption spectrometry measurements of X52 specimens and the API weldment specification for X52 grade steel are given

Material	***Carbon (%)***	***Manganese (%)***	***Phosphorus (%)***	***Sulfur (%)***	***Titanium (%)***
X52 Tested Steel	0.061	1.31	0.005	0.0069	--
	0.0609	1.30	0.004	0.0069	--
	0.0606	1.31	0.005	0.0073	--
API X52 - Weld PSL2	0.22 max.	1.40 max.	0.025 max.	0.015 max.	0.04 max.

Table 2a. Optical emission spectroscopy measurements and Leco Carbon/Sulfur analysis of X52 specimens, and the API specification for X52 grade steel are given.

	OES	AAS	LECO	API Specification	
C	0.154	0.061	0.081	0.300	Max
S	0.006	0.007	0.001	0.050	max
P	0.011	0.005	N/A	0.040	max
Mn	1.098	1.31	N/A	1.350	max
Si	0.217	N/A	N/A	N/A	
Cr	0.072	N/A	N/A	N/A	
Ni	0.019	N/A	N/A	N/A	
Cu	0.014	N/A	N/A	N/A	
Mo	0.008	N/A	N/A	N/A	
Ti	0.021	N/A	N/A	N/A	
Al	0.045	N/A	N/A	N/A	
V	0.030	N/A	N/A	N/A	
Co	0.007	N/A	N/A	N/A	
W	0.004	N/A	N/A	N/A	
B	0.001	N/A	N/A	N/A	
Sn	0.021	N/A	N/A	N/A	
Pb	0.009	N/A	N/A	N/A	

Table 3. Optical emission spectroscopy measurements, Leco Carbon/Sulfur analysis, and the API specification for X65 grade pipeline steel.

	OES	LECO	API Specification
C	0.09	0.063	0.100 Max
S	< 0.01	0.0025	0.005 max
P	0.01	N/A	0.015 max
Mn	1.50	N/A	1.50 max
Si	0.31	N/A	0.35 max
Cr	0.03	N/A	N/A
Ni	0.23	N/A	N/A
Cu	0.15	N/A	N/A
Mo	< 0.01	N/A	N/A
Ti	0.021	N/A	N/A
Al	0.045	N/A	N/A
V	0.030	N/A	Controlled
Co	0.007	N/A	N/A
W	0.004	N/A	N/A
B	0.001	N/A	N/A
Sn	0.021	N/A	N/A
Pb	0.009	N/A	N/A

Table 4. Atomic absorption spectrometry measurements and the API specification for X70 grade pipeline steel.

Material	***Carbon (Wt. %)***	***Manganese (Wt. %)***	***Phosphorus (Wt. %)***	***Sulfur (Wt. %)***	***Titanium (Wt. %)***
X70 Tested Steel	0.074	1.41	0.012	0.0029	--
	0.0655	1.41	0.005	0.0033	--
	0.0718	1.42	0.012	0.0031	--
API X70 - Weld PSL2	0.22 max.	1.65 max.	0.025 max.	0.015 max.	0.06 max.

Table 5. Atomic absorption spectrometry measurements and the API specification for X80 grade pipeline steel.

Material	***Carbon (Wt. %)***	***Manganese (Wt. %)***	***Phosphorus (Wt. %)***	***Sulfur (Wt. %)***	***Titanium (Wt. %)***
X80 Tested Steel	0.06975	1.34	0.004	0.0040	0.012
	0.06957	1.35	0.004	0.0040	0.009
	0.07342	1.36	0.004	0.0030	0.008
API X80 - Weld PSL2	0.22 max.	1.85 max.	0.025 max.	0.015 max.	0.06 max.

3.1.2 Metallography

Optical microscopy for X52, X65, X70, and X80 grade pipeline steels are shown in the figures below. The micrograph of a transverse X52 section exhibits a ferritic structure with small pockets of pearlite, which indicates a low carbon content (hypoeutectoid) steel. The ferrite grain size ranges from approximately 5 – 20 microns.

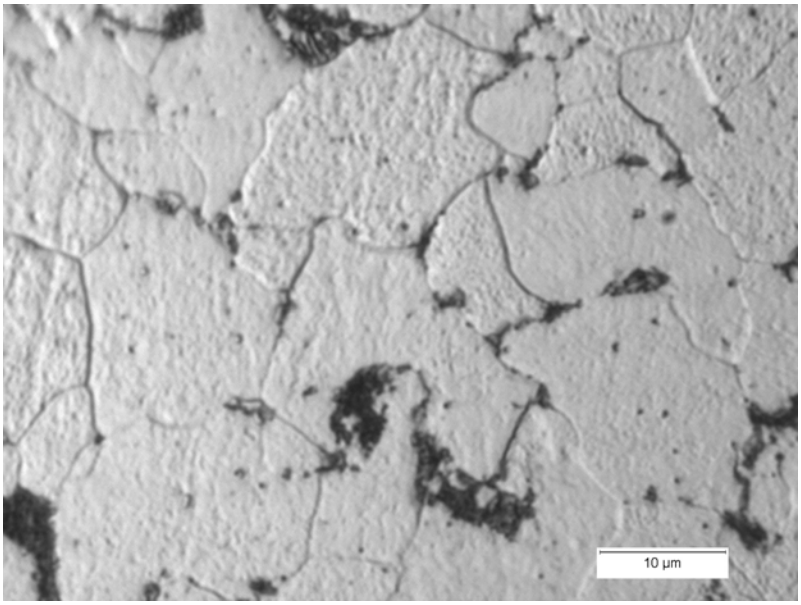

Figure 2 - X52 pipeline steel micrograph indicating largely ferritic grain structure with small pockets pearlite formation at grain boundaries.

Figure 3 is a longitudinal micrograph of X65 grade steel illustrating a ferritic structure with drawn-out stringers of pearlite, which indicates a low carbon content (hypoeutectoid) steel.

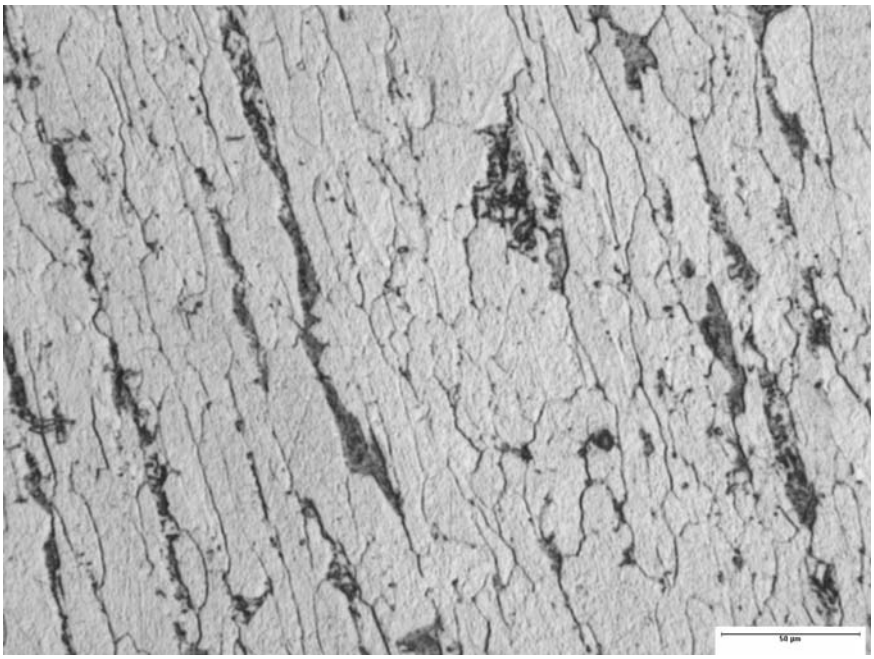

Figure 3 – Longitudinal section of X65 grade pipeline steel showing micrograph ferritic structure with drawn-out stringers of pearlite.

Figure 4 and 5 are transverse and longitudinal micrographs, respectively, of X70 grade pipeline steel exhibiting a fine-grain structure of low carbon content steel with a small amount of precipitated carbides at the grain boundaries. The refined grain size contributes to higher-

strength when compared to the X52 and X65 grade steel micrographs. The elongated grain structures due to rolling and processing are most evident in the longitudinal specimens at lower strengths such as the X65 and X70 steels.

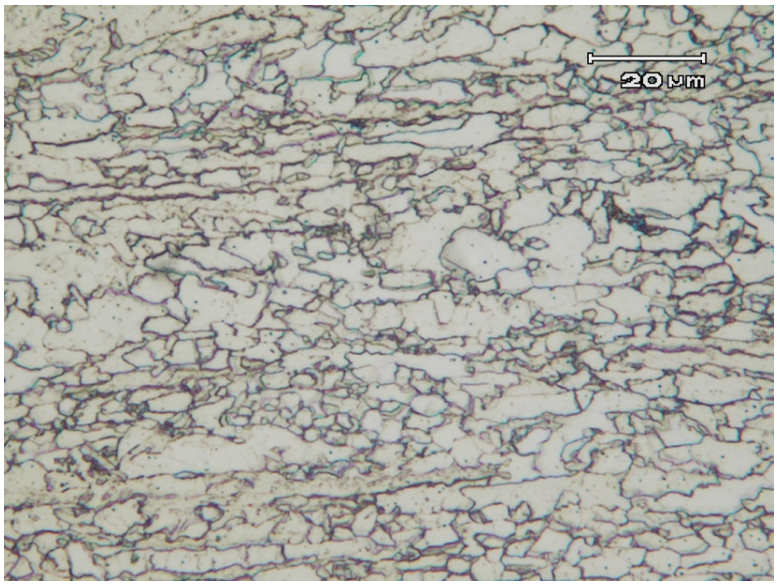

Figure 4 – Longitudinal specimen of X70 showing a refined grain structure.

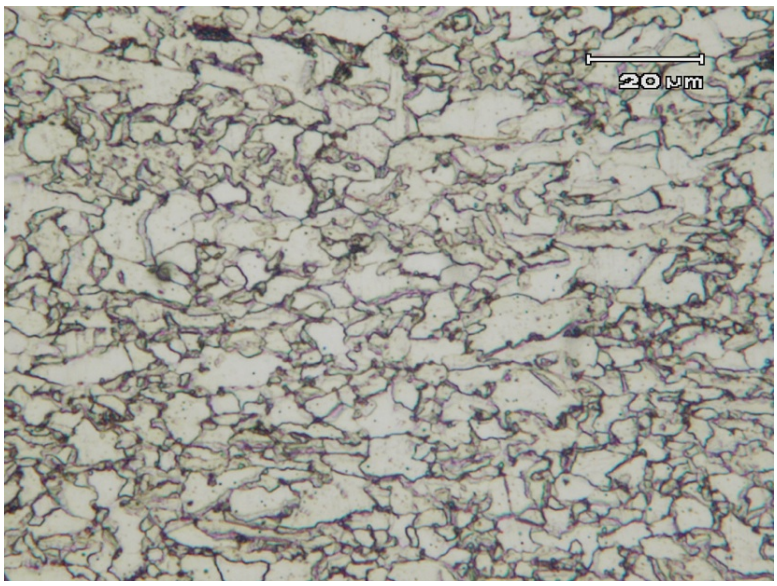

Figure 5 – Transverse section of X70 grade pipeline steel exhibiting a fine grain microstructure.

Figure 6 is a transverse micrograph of X80 steel illustrating a fine irregular ferritic structure with some evidence of precipitated carbides assisting in strengthening. The microstructure appears to be higher-strength with sufficient toughness as compared to the X52, X65, and X70 grades of pipeline steel. The microstructures of these pipeline steels are very consistent with the measured compositions, with the recognition that processing parameters such as cooling rates will also contribute to the microstructural features.

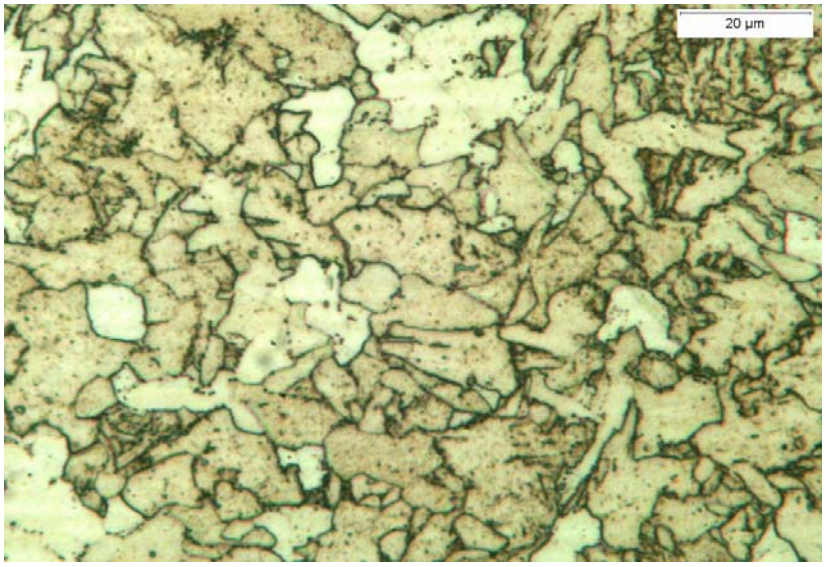

Figure 6 – Transverse section of X80 grade pipeline steel exhibiting an irregular fine grain ferritic structure with some precipitates at grain boundaries.

3.1.3 Mechanical Properties Assessment

Tensile and microhardness tests were performed to assess the mechanical properties of X52, X65, X70, and X80 grade pipeline specimens in the CSM mechanical properties testing laboratory. The results presented in Table 6 include the tensile or microhardness evaluation of these steels and exhibits strengths that are typically fifteen to thirty percent above the specified minimum.

These measured strengths of the X52, X65, X70, and X80 pipeline steels are all well in excess of the API 5L specification for mechanical properties. The order of reported strengths for these steels are consistent with the microstructures analyzed above. There is insufficient chemical analysis for the X70 and X80 grade pipeline steels to establish a correlation of mechanical properties and compositions.

Table 6. Yield stress results from tensile test measurements of X52 longitudinal, X65 longitudinal, and X65 lateral pipeline steel tensile specimens.

Sample Type	2% Offset Yield Strength (psi)	API Spec Yield Strength	Ultimate Tensile Strength (psi)	API Spec UTS Strength
X52 longitudinal	59,700	52,000	72,400	66,000
X52 longitudinal	56,200	52,000	69,600	66,000
X52 longitudinal	60,100	52,000	72,900	66,000
X65 lateral	84,900	65,000	94,500	77,000
X65 lateral	83,900	65,000	93,600	77,000
X65 lateral	84,300	65,000	93,400	77,000
X65 longitudinal	77,800	65,000	90,000	77,000
X65 longitudinal	77,500	65,000	89,100	77,000
X65 longitudinal	78,300	65,000	90,900	77,000
X70 longitudinal	81,900	70,000	94,900	82,000
X70 lateral	83,400	70,000	93,400	82,000
X80 (hardness)	Hardness = HV 207 or HRB 94	80,000	Approximately 100,000	90,000

4.0 INITIAL WORK

The main objective of the initial work done by Sanchez at CSM was to describe experimentally the effect of high strength magnetic fields applied during pigging operations to steel pipeline on the hydrogen-induced cracking susceptibility and quantitatively measure the increased hydrogen activity in thick walled, high strength steels due to the magnetization (Sanchez, 2005).

Sanchez found that the presence of a magnetic field during the cathodic charging of high strength linepipe steels resulted in an increase in hydrogen absorption Figure 7 (Sanchez, 2005).

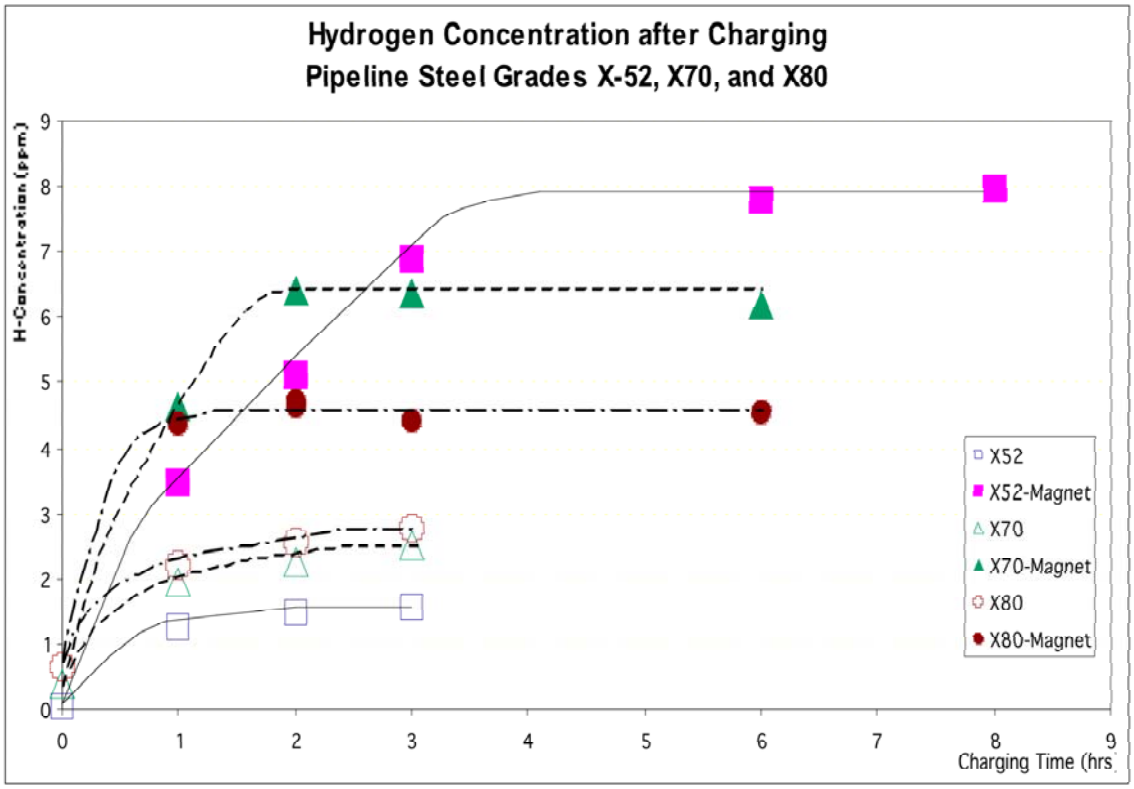

Figure 7: Plot of hydrogen concentration versus charging time (hrs). Plot shows an increase in hydrogen absorption in the presence of a magnetic field for all steel grades tested (X52, X70, X80).

Sanchez also found that increased hydrogen absorption lead to an increase in pitting and cracking of the steel samples as shown below in Table 7.

Table 7: Hydrogen induced cracking results for X70 and X80 [4].

Charging Time (hours)	Pipeline Steel Grade X70				Pipeline Steel Grade X80			
	Pitting		Cracks		Pitting		Cracks	
	Non-Magnet	Magnet.	Non-Magnet	Magnet	Non-Magnet.	Magnet	Non-Magnet	Magnet
12	Minor	Moderate	No	Yes	n/t	No	n/t	No
24	Minor	Heavy	No	Yes	No	Minor	No	Yes
36	n/t		n/t		Minor	Heavy	No	Yes

Further evidence of pitting and cracking is shown below in an SEM image of an X80 steel Figure 8.

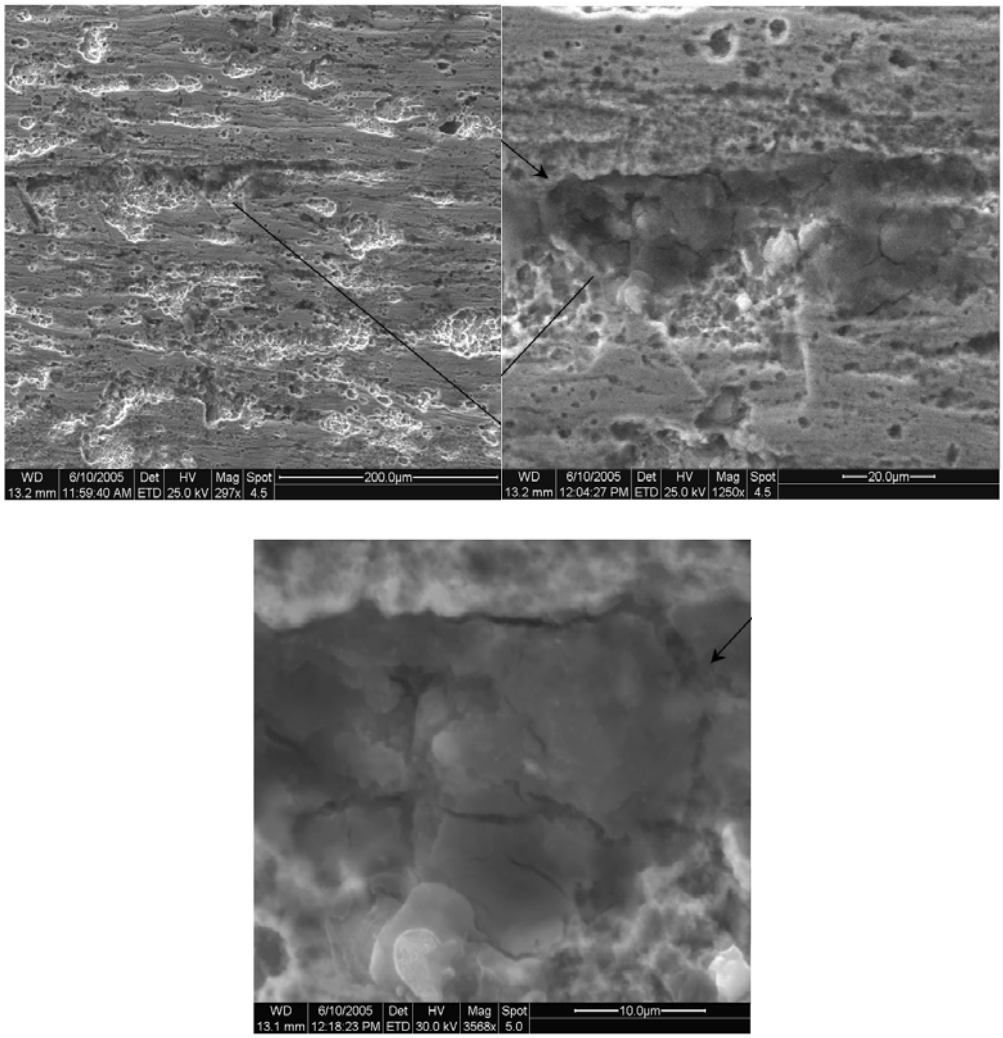

Figure 8: SEM image of X80 showing pitting and cracking behavior after 24 hours of charging.

Further work is ongoing at CSM to confirm the results obtained by Sanchez and also aims to determine a mechanistic understanding of increased hydrogen absorption, and magnetocorrosion, which is corrosion in the presence of a magnetic field. The details of the current research are given below.

5.0 CURRENT WORK

Electrochemical cathodic charging and electrochemical impedance spectroscopy are being utilized to assess and understand the nature of magnetocorrosion on pipeline steel. Significant modifications to the experimental arrangements have been made to achieve a consistent high-accuracy assessment capability, and experimental tests indicate good correlation with previous research and offer new insight into the complex phenomena occurring.

6.0 EXPERIMENTAL ARRANGMENT

New experimental arrangements have been designed for this phase of the project. Significant changes have been made to the sample holder assembly and to the manner in which the magnets are controlled and isolated from the solution, as illustrated in Figure 9.

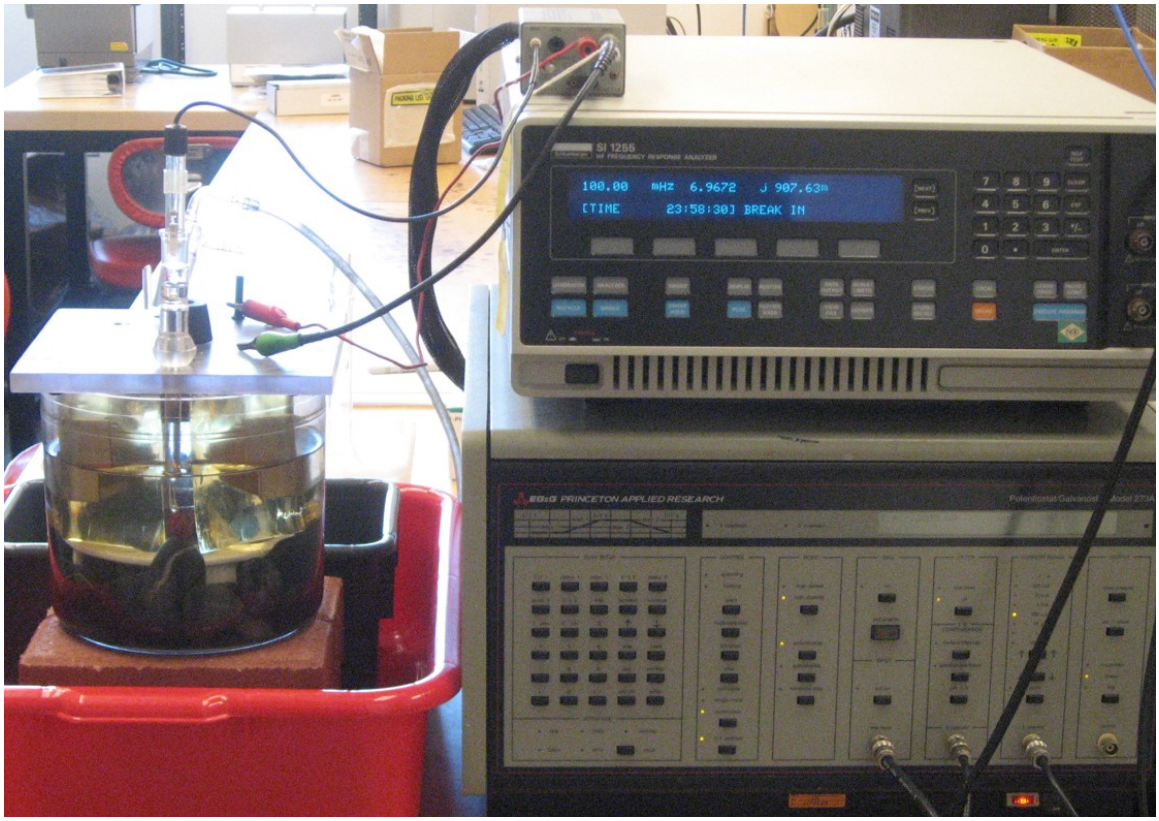

Figure 9 -: Hydrogen charging experimental system. On the left hand side of the figure is the electrolytic hydrogen charging cell and on the right hand side is the Princeton Applied Research Potentiostat/Galvanostat Model 273A.

The hydrogen charging system consists of the electrolytic cell and the Princeton Applied

Research Potentiostat/Galvanostat Model 273A. The electrochemical impedance spectroscopy arrangement combines the cathodic charging arrangement with the use of the Schlumberger Research Instruments (now Solartron Analytical) 1255 HF Frequency Response Analyzer to perform impedance analysis.

6.1 Electrolytic Cell

The electrolytic cell contains the steel sample, two magnet towers mounted in epoxy resin (utilized to achieve varying magnetic field strengths), a graphite anode rod, and the Standard Calomel Electrode (SCE) reference electrode. Each magnet tower produces a continuous magnetic field as large as 1.6 Tesla (T). The magnet towers are mounted inside an epoxy resin case that provides isolation from the sulfuric acid solution. All of the components of the cell are explained in detail below.

6.1.2 Magnet Epoxy Mount

To isolate the magnets from the sulfuric acid solution the magnets were mounted in Buehler Epothin epoxy resin, as shown in Figure 10. Buehler Epothin is a two-part epoxy resin typically used for cold-mounting metallurgical samples in preparation for optical microscopy. Buehler Epothin is a low viscosity fluid that forms a strong, leak proof bond between itself and the material that it surrounds. Epothin is an ideal material in which to mount the magnets because it is chemically resistant to most solvents.

Mounting the magnets in Buehler Epothin served two purposes. First, the epoxy resin provided a means of isolating the magnets from the sulfuric acid. And secondly, the epoxy acted as a housing that could be used to maintain an accurate distance between the magnet faces. The distance between the magnet faces is held constant for each experiment by the use of spacers, as can be seen in Figure 10. The spacers are made either of the two-part epoxy resin or Viton o-rings both of which are chemically resistant to sulfuric acid. The spacer design is utilized to allow for the magnetic field intensity to be varied by increasing or decreasing the separation distance between the magnet faces or by utilizing various strength pyramidal magnetic arrangements to achieve further variation of the magnetic field.

6.1.3 Magnet Mount Process

To ensure that the magnets are completely isolated from the sulfuric acid the mounting process must be done in steps. An insulating base layer of epoxy resin must be poured initially, which is 0.25 in. (6.35 mm) thick, and upon which the magnet assembly sits. After the base layer cures completely, the magnet assembly is placed in the center of this layer, and the next layer is poured. The second layer and each successive layer are approximately one inch thick. Given the size of the container in which the magnets were mounted, shown in Figure 11, it was determined that if a layer of epoxy exceeded about one inch thickness the layer would never fully solidify. Complete solidification, regardless of layer thickness (up to the one inch limit), requires about nine hours. If complete solidification is never achieved, which may also occur due to improper mixing or residual moisture in the mounting container, the epoxy will have a consistency similar to silly putty or jello. A layer that is not completely solidified will result in poor bonding with the subsequent layer, and ultimately lead to an epoxy mount that does not enable complete isolation of the magnet from the solution. Each mount consists of approximately five layers of epoxy;

therefore, the entire mounting process for each magnetic arrangement requires approximately 45 hours of preparation time.

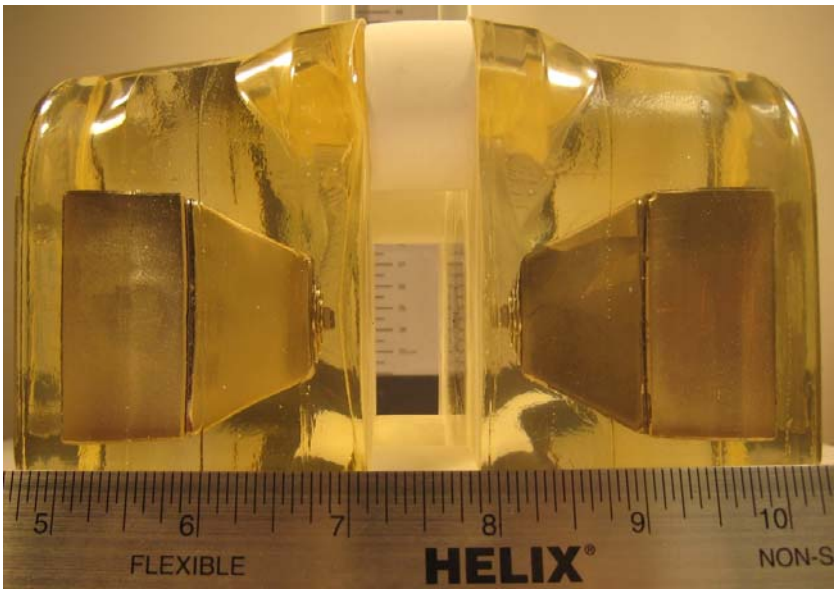

Figure 10 -The magnets can be seen inside the epoxy resin. The white cylinders between the epoxy mounts act as spacers that can be fabricated to any desired dimension.

6.1.4 Magnet Assembly

The magnets mounted inside the epoxy resin, shown in Figure 4, are made of neodymium. Each magnet assembly or tower is comprised of three neodymium parts. The base, the pyramid, and a magnet stack. The base is a 2 in. x 2 in. x 1 in. (50.8 mm x 50.8 mm x 25.4 mm) rectangle of neodymium, the pyramid has a 2in. x 2in. (50.8mm x 50.8 mm) base and tapers to a 1 in. x 1 in. (25.4mm x 25.4 mm) square and is 1 inch (25.4 mm) thick, the magnet stack consists of a series of magnets with successively smaller surface areas with the smallest magnet having square dimensions of 4 mm x 4 mm. All of the neodymium magnets have a thin nickel plating to prevent the oxidation of neodymium. This magnet-stacking configuration was utilized to create an approximate static magnetic field of 1 Tesla at the center of the field.

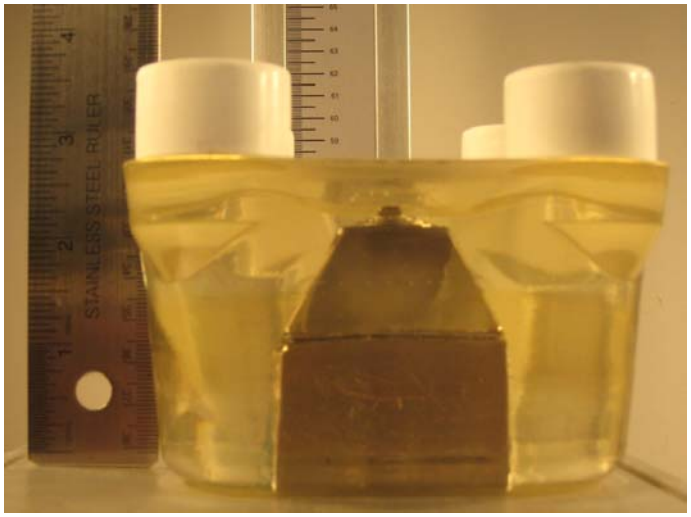

Figure 11 – The side profile of the magnet assembly tapering from the base down to a 4 mm x 4 mm magnet square.

6.1.5 Sample Geometry

The steel samples of type X52, X65, X70, and X100 have been machined into cylindrical shell geometry specimens. All steel samples were machined to the same specifications and dimensions. The cylinders have an outer diameter of 0.25 in. (6.35 mm) and an inner diameter of 0.0781 in. (1.984 mm) and a length of 0.25 in. (6.35 mm) giving a surface area of 251.6 mm^2. Machining a hole through the center of the sample allows for the sample to be completely cleaned of all machining oil and provides a means for electrical contact when the sample is being charged. All have samples have approximately the same mass (m = 1.5 g).

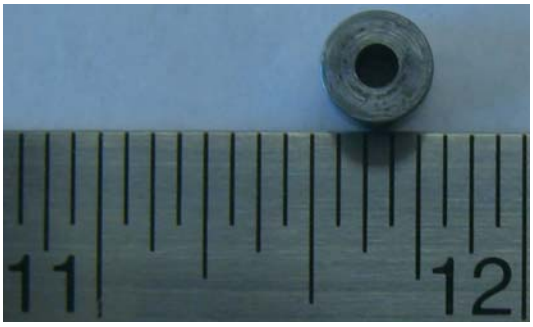

(a)

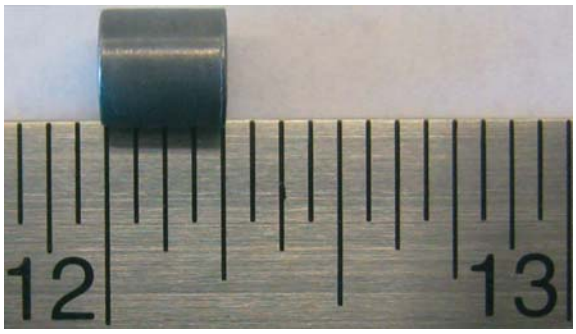

(b)

Figure 12 -X52 grade pipeline steel specimen with 6.35 mm diameter and length for use in hydrogen charging experiments in the (a) top down and (b) side profile views.

6.1.7 Sample Holder Design

Isolation of the electrical contact from the sulfuric acid proved to be a significant challenge for making accurate measurements. A modified Stern-Makrides assembly [2] was used in the experiments to obtain a leak proof seal around the electrical contact. In a regular Stern-Makrides assembly, the electrode is tapped, threaded, and attached to a stainless steel rod through a Teflon washer [3]. The stainless steel rod is isolated from the solution with a heavy-wall glass tube and the assembly is made leak proof by tightening a nut at the top of the steel rod [3]. However, due to concerns over tapping oil contamination, the electrode used in the experiments for this project had to be modified for use without threading (in which trapped residual oil and other contaminants may be very challenging to completely remove). Heretofore, the steel samples were machined as described above, and a new electrode mounting assembly was designed. The modified sample holder consists of three parts: A type 316 stainless steel rod, compression fitting, and a Teflon gasket. All materials used in the sample holder are non-magnetic and chemically resistant to sulfuric acid. The components of the sample holder are explained below in detail.

6.1.8 Stainless Steel Rod

The stainless steel rod serves two purposes in the sample holder arrangement: (1) to hold the sample in place between the magnets, and (2) to act as an electrical contact for the sample. Stainless steel was chosen as the material to hold the sample because it is non-magnetic. The rod is 20 cm in length and is threaded at both ends. The end of the rod on which the sample is placed has a diameter of 1.98 mm with a thread spacing of forty-eight threads per inch and a length of 3 cm. On the opposite end of the rod, which is connected to the electrometer, has a thread spacing of thirty-two threads per inch and has a diameter of 4.365 mm.

6.1.9 Compression Fitting

Modifications made to the original Stern-Makrides assembly altered the manner in which the electrode was connected to the stainless steel rod. Since the altered arrangement uses no threads in the working electrode specimen, a compression fitting was designed as a means of attaching the electrode to the steel rod. The compression fitting is threaded onto the finely threaded end of the stainless steel rod and compresses the sample between two Viton o-rings and another Teflon gasket. The compression created by the fitting results in a leak proof seal around both ends of the sample, Figure 7.

6.2 Compression Fitting Design

The compression fitting consists of three parts: an epoxy resin housing, a threaded type 316 stainless steel base, and a Teflon gasket. Epoxy resin was used as the housing material because it is chemically resistant to sulfuric acid, forms a leak proof seal around the steel/Teflon stack, and is easily machined. The epoxy housing for the compression fitting was made in a similar fashion to that of the magnet epoxy mounts. A thin base layer of epoxy is poured, and then a second layer is poured to completely isolate the stainless steel and Teflon from the solution. Figure 13 shows how the stainless steel and Teflon gasket are stacked inside the epoxy housing giving a leak proof seal. The entire compression fitting is approximately an inch in length and a half an inch in diameter.

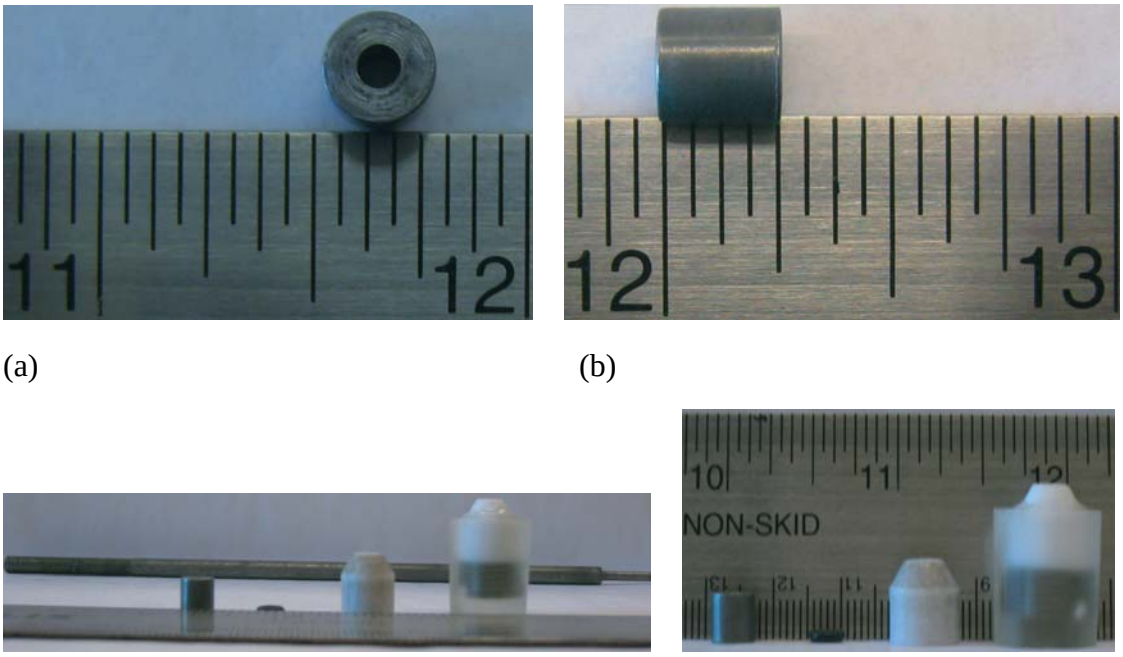

(a) (b)

(c) (d)

Figure 13 -The specimen and sample holders shape and size are illustrated in Figures 5 (a) - (d) to give an idea of the size of the parts (Teflon gasket, Viton o-ring, and sample) associated with the sample holder. In Figure 5 (b), notice on the right hand side of this image that the stainless steel rod decreases in diameter from 0*:*1875 in*:* (4*:*76 mm) to a diameter of 0*:*0781 in*:* (1*:*984 mm). This section of rod is inserted through the Teflon gasket, Viton o-ring, and sample (which screw together) as in image (d).

7.0 HYDROGEN CHARGING SOLUTION CHEMISTRY

Cathodic charging of the steel samples was performed in a 1 N H_2SO_4 sulfuric acid solution. Acid, such as sulfuric, that contain more than one dissociable proton are called polyprotic acids. Polyprotic acids dissociate in a stepwise manner, and each dissociation step is characterized by its own acid-dissociation constant, K_{a1}, K_{a2}, and so on [1]. Taking sulfuric acid as an example, the following dissociation reactions can be formed:

$$H_2SO_4 + H_20 = H_30^+ + HSO_4^-$$

Leading to the first acid dissociation constant:

$$K_{a1} = \frac{\left[HSO_4^-\right]\left[H_30^+\right]}{H_2S0^4}$$

K_{a1} is a very large number and therefore makes sulfuric acid a strong acid. Equation 1 describes the dissociation of sulfuric acid to bisulfate HSO_4^-. The second dissociation reaction is the bisulfate ion, HSO_4^-, going to sulfate SO_4^{2-}:

$$HSO_4^- + H_2O = H_3O^+ + SO_4^{2-}$$

This reaction provides the second and last acid-dissociation constant for sulfuric acid:

$$K_{a2} = \frac{\left[SO_4^{2-}\right]\left[H_3O^+\right]}{\left[HSO_4^-\right]} = 1.2\,x10^{-2}$$

The values of stepwise dissociation constants of polyprotic acids typically decrease, usually by a factor of 10^4 to 10^6 for each dissociation step. This behavior arises due to electrostatic forces that make it far more difficult to remove a positive proton from a negative ion such as HSO_4^- than from a molecule that is uncharged such as H_2SO_4[1].

7.1 Solution Concentration Calculation

The sulfuric acid solution is made in five gallon batches. Making large batches of the solution ensures a homogeneous solution between experiments. The details of making a $1N\,H_2SO_4$ solution are given below. The five-gallon batches of $1N\,H_2SO_4$ solution are mixed according to the determined concentration, as follows:

$$1M = mass / L / GFW$$

$$1N = 1M * Z$$

Where Z is the number of liberated hydroxide ions, M is the molarity, and N is normality of the solution:

$$1M = mass / L /(98)$$

$$1N = 1M * Z \text{ (sulfuric acid = 2)} = mass / L /(49)$$

The liquid density of the reagent grade sulfuric acid is 1.84 g/cm^3. This density value gives a final concentration of:

$$1N\,H_2SO_4 = \frac{49}{1.84} = 26.6\frac{cm^3}{L}$$

Given the above information, the amount of sulfuric acid that must be utilized to make a five-gallon batch of 1 normal sulfuric acid solution can be calculated.

$$1\ cm^3 = 1\ mL$$

$$5\ gallon \cdot \frac{4\ qt}{1\ gallon} \cdot \frac{1\ L}{1.075\ qt} = 18.92\ L$$

$$26.6\ \frac{cm^3}{L} \cdot 18.92\ L = 503.2\ cm^3$$

$$503.2\ cm^3 \cdot \frac{1\ mL}{1\ cm^3} = 503.2\ mL \approx 0.5\ L$$

Therefore, for a $1N\ H_2SO_4$ solution, 0.5 L of concentrated sulfuric acid needs to be utilized in five gallons of water.

8.0 SAMPLE PREPARATION

To prepare the samples for hydrogen charging the following procedure is used.

1. The steel samples are placed in a beaker of Trichloroethylene for about thirty minutes. Trichloroethylene is a chlorinated hydrocarbon commonly used as an industrial solvent. Trichloroethylene is an effective solvent for many organic compounds and is used as a metal degreaser. Trichloroethylene was found to be the most effective solvent for removing the machining oil from the samples.
2. After soaking in the Trichloroethylene, the samples are then placed in a furnace at a temperature of $400^\circ C$ for one hour. This step is done to drive off any residual hydrogen in the steel sample. The samples are removed from the furnace and allowed to air cool.

Typically, about twenty samples are placed in the Trichloroethylene and then baked in the furnace. Therefore, the procedure listed above could be considered the bulk sample preparation procedure. The individual sample preparation procedure is given below.

1. When the sample is cooled to room temperature, return to Trichloroethylene bath for about ten minutes.
2. Remove the sample from the Trichloroethylene and allow time for the Trichloroethylene to evaporate.
3. Grind sample down to 600 grit on all faces, dry the sample off with compressed air.
4. Place sample in Trichloroethylene again for about five minutes
5. Repeat step three, put the sample back in the Trichloroethylene, remove sample from the Trichloroethylene, allow time for Trichloroethylene to evaporate and cover with a cotton ball. This last step is done to ensure that any residual water is removed from the sample after the last polishing and grinding step.

9.0 HYDROGEN CONCENTRATION DETERMINATION

After the steel samples are charged with hydrogen, the hydrogen content was measured with the LECO Hydrogen Determinator RH-404 (Figure 14).

Figure 14 - LECO Hydrogen Determinator RH-404. On the left is the unit that measures that hydrogen concentration and on the right is the electrode furnace.

The weight and dimensions of the steel sample used for testing is limited by the requirements of the hydrogen determinator. Typical values of sample weight range for the Leco hydrogen determinator is 0.5 - 1.5 grams while the maximum diameter is 0.295 in. (7.49 mm) and the maximum length is 0.708 in. (17.9 mm). To calibrate the LECO Hydrogen Determinator RH-404, three steel standard calibration samples with approximately $6.0 \pm 0.2\ ppm$ hydrogen were used before any charged samples were tested in the electrode furnace.

10.0 HYDROGEN CHARGING EXPERIMENTAL PROCEDURE

A series of cathodic hydrogen charging experiments were carried out on X52 grade steel. For the hydrogen charging experiments, the steel samples were prepared having a surface area of 2.516 cm^2. Each steel sample was ground to 600 grit on SiC grinding paper and cleaned in trichloroethylene to remove any residual hydrogen from the machining process.

The hydrogen charging experiments were performed in an electrolytic cell, under potentiostatic conditions, containing a solution of $1N\,H_2SO_4$. For each experiment, fresh solution was used, and prior to beginning a new experiment the cell was thoroughly cleaned. Hydrogen absorption into the steel samples was induced by a constant cathodic potential of -0.550 V. The Hydrogen charging experiments ranged in duration from 0 hours to 16 hours (0, 2, 4, 8, 12, 16). A series of six experiments would be performed under the influence of an approximate static magnetic field of 0.6 T and then another series of six experiments would be performed without the magnetic field.

The samples used for the measurement of hydrogen concentration, were cylindrical in shape, and had the following dimensions: D=0.25 in. (6.35 mm) and length l=0.25 in. (6.35 mm). Upon completion of charging, the samples were taken to the LECO RH-404 Hydrogen Determinator, for hydrogen concentration analysis.

11.0 RESULTS AND DISCUSSION

To determine the effect of a magnetic field on hydrogen content in pipeline steel, a series of cathodic hydrogen charging experiments were performed on steel grade X52. A series of experiments was run with a magnetic field of 0.6 T and second series without the influence of a magnetic field. The hydrogen concentration as a function of charging time is plotted in Figure 15. At the surface of each magnet mount, a magnetic field of approximately 1 T was measured. However, with a separation distance of 0.5 inches (12.7 mm) between the magnet face, the magnetic field strength is 0.6 T.

The results indicate that a magnetic field has a significant effect on the amount of absorbed hydrogen concentration in pipeline steel. The results obtained from the experiments completed during this research are in good agreement with the experimental results obtained by Sanchez (Sanchez, 2005).

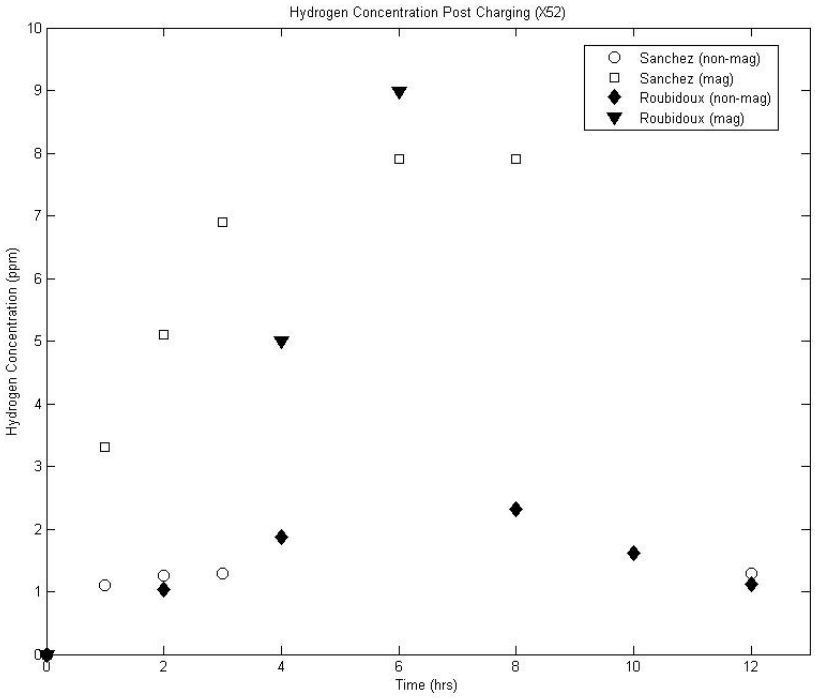

Figure 15: Comparison of Roubidoux and Sanchez hydrogen charging data.

12.0 BUBBLE FORMATION AND BUBBLE FLOW

Observations made during experimentation revealed that bubbles typically nucleated at the bottom edge of the sample, would grow to a certain size, and migrate to the top of the sample. During the initial stages of an experiment the bubbles that nucleated were rather large and would cover a significant amount of sample surface area.

Bubble formation was dependent on the presence of a magnetic field. If there was no influence from the magnetic field the nucleation and growth of large bubbles on the sample surface would proceed for approximately 1000 seconds. If the magnetic field was present, the nucleation and

growth of large bubbles would proceed for approximately 500 seconds. After these times bubble formation would reach what could be considered steady state. Steady state is characterized by a significant decrease in bubble size and the formation of a thin, flowing bubble layer. In the unsteady condition, bubble size could reach diameters as large as 0.125 inches (3.175 mm).

Upon the establishment of steady state, two different flow paths were observed, which are dependent on the presence of a magnetic field. With no influence from a magnetic field, the bubbles would nucleate at the bottom of the sample and flow directly up the sample. However, once a magnetic field is introduced, the bubble flow path is altered and the flowing bubble layer is more diffuse. Under the influence of a magnetic field, the bubbles follow a helical flow pattern up and around the sample.

Bubble nucleation occurs according to the classical theories of nucleation, in which a critical radius of atoms is required to nucleate before the nucleation and growth can proceed. The pressure of bubble nucleation, P_g, must exceed the sum of the surface tension and curvature, P_c, Pressure balance with atmospheric pressure, P_a, and Hydrostatic force (depth of bubble), P_h.

In the absence of a magnetic field, bubble formation occurs and bubbles flow directly up the sides of the cylindrical sample. In the presence of a magnetic field, bubble flow is noticeably decreased and flows helically outward towards to the magnets on either side of the specimen.

13.0 MAGNETOCORROSION – PITTING AND CRACKING TESTING

Pitting and cracking corrosion tests are to be performed using the finalized hydrogen charging and impedance measurement system. Residual strain will be simulated by use of controlled-rolled pipeline steel specimens to allow quantitative estimation of the residual stress. A comprehensive experimental matrix will be performed to assess the important parameters related to residual stress, pitting, and cracking of pipeline steel.

13.1.1 Investigation of Mechanistic Interpretations of Magnetocorrosion

Modeling of the underlying effects of magnetocorrosion behavior has coupled electromagnetic perturbations to alterations in the electrochemical behavior, including the Helmholtz and Gouy-Chapman layer. These perturbations result in enhanced anodic and cathodic behavior, resulting in both increase in hydrogen ingress and pitting and cracking behavior. The mechanistic description has been presented in the references below.

Possible thermodynamic explanations of the observed effect of magnetization on hydrogen content have been developed. The Helmholtz Free Energy was selected as the proper description of the effect of magnetization on the interaction of a combination of internal and external work contributions to a thermodynamic system. The electrochemical work and the external work performed on the system are traditionally represented by the Gibbs Free Energy and Nernst equations. The magnetization influence on the electronic spin configurations is considered as an internal work contribution. The effect of magnetostriction, the directional strain induced in steel from an applied magnetic field, and interstitial solute-induced strain are considered as volume-change terms.

The log of the hydrogen solubility is given in equation 3:

$$\ln[H] = \frac{F\mathcal{E}}{RT} - \frac{\delta w_{\text{int}}}{RT} - \frac{PdV_{MS}}{RT} - \frac{PdV_{Sol}}{RT} - \frac{\sum \mu^{o}{}_{i} n_i}{RT} - 2.3pH \quad (3)$$

Equation 4 gives the hydrogen solubility for the electrochemical reaction as a function of pH, temperature, electrochemical potential, and alloy contents:

$$[H_B] = [H]_{B=0} \exp\left[\frac{\Delta MB}{RT}\right] \exp[\frac{PdV_{MS}}{RT}] \exp[\frac{PdV_{Sol}}{RT}] \quad (4)$$

where the hydrogen concentration with no magnetic field ($[H_{B=0}]$) is:

$$[H]_{B=0} = \exp[2.3pH] \exp[\frac{-\sum \mu_i{}^{o} n_i}{RT}] \quad (5)$$

Equation 6 includes the modeled effects of spin magnetization, magnetostriction, and solute-strain on the thermodynamics of hydrogen in a ferrous material. The amplifying effects of the exponentials are such that magnetization only significantly alters the hydrogen solubility if the magnetostriction term is positive (promoting lattice tensile strain), as seen in equation 6:

$$[H_B] = [H]_{B=0} \exp\left[\frac{\Delta MB}{RT}\right] \exp[\frac{\pm M_s{}^2 \mu_o{}^2 \mathrm{H}^2}{9\lambda_s{}^2 YRT}] \exp[\frac{\frac{2}{3}\mu\frac{1}{\Omega}(\frac{d\Omega}{dc})^2 f(c)}{RT}] \quad (6)$$

The square of the magnetic field strength in the exponential magnetostriction work term further amplifies the effect of Magnetostriction work on hydrogen solubility. Further details of these calculations are included in the International Journal of Thermophysics and Offshore Mechanics and Arctic Engineering.

13.1.2 Kinetic Model

At the interface between steel and the transported liquid two layers exist that limit the adsorption and transport of hydrogen ions. The Helmholtz Double Layer (HDL) is a capacitor-like separation of cation and anion charges. In additions to this compact layer, there exists a diffuse layer known as the Gouy-Chapman Layer (GCL) in which the concentration of ions near the charged surface is reduced to some degree, altering the availability of ions to be reduced and absorbed. These layers act to limit the diffusion of hydrogen content into steel and therefore limit the hydrogen content. In the event of breakdown or disturbance of these layers, increased diffusion occurs and hydrogen supersaturation may occur.

Cathodic protection or an applied magnetic field leave these layers essentially undisturbed when applied separately. However, the application of cathodic protection currents in the presence of remanent magnetic fields leads to the creation of Larmor loops. Electromagnetic waves

propagate approximately perpendicular to metal surfaces, independent of the incident angle, leading to higher surface fields. During the interval when the magnetic field is dominant, electrons move in “Larmor loops” due to the interaction of the electron charge and the magnetic field, creating a cross-product (VxB) force that create looping orbits in the conduction band electrons in the metal. Sample thickness, applied current, and external magnetic fields all contribute to the oscillating current and voltage conditions which occur at the surface as described in Makarov (1995). Figure 16 shows the effect of Larmor electrons in disturbing the metal-side of the HDL and induced Larmor electrons disturbing the electrolyte-side of the HDL and GCL.

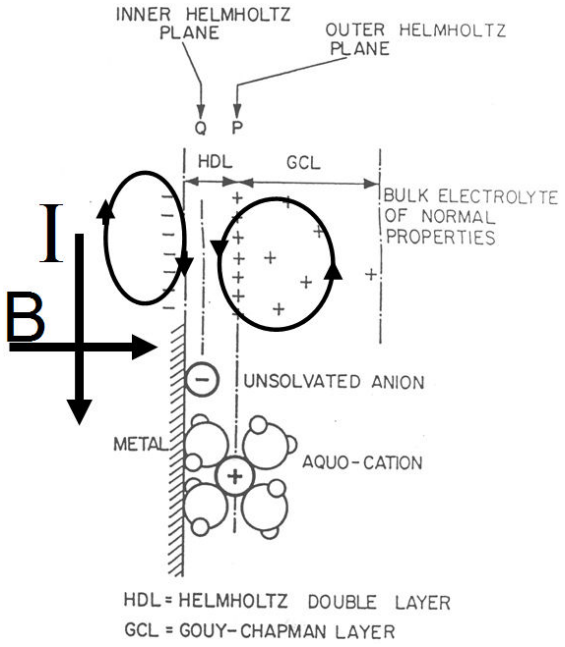

Figure 16. Illustration of Helmholtz Double Layer and Gouy-Chapman Layer, including Larmor Loop effects from combined electrical and magnetic fields.

Magnetism will cause Lorentz forces to stir the moving ions in the electrolyte passing within a pipeline. Sufficiently high magnetic fields, such as may be remanent after magnetic flux leakage, may create a sufficient Lorentz force to stir the electrolyte and increase the limiting exchange current density. Without any magnetic or electrical fields, corrosion occurs at a rate i_{corr}, where the lines for hydrogen reduction and iron oxidation cross on the Evans diagram. Cathodic protection increases the rate of hydrogen production while decreasing the corrosion current. Disturbance of the HDL will increase the exchange current and thus shift the polarization curve to greater currents, increasing hydrogen content as well as the corrosion current, as shown in Figure 17.

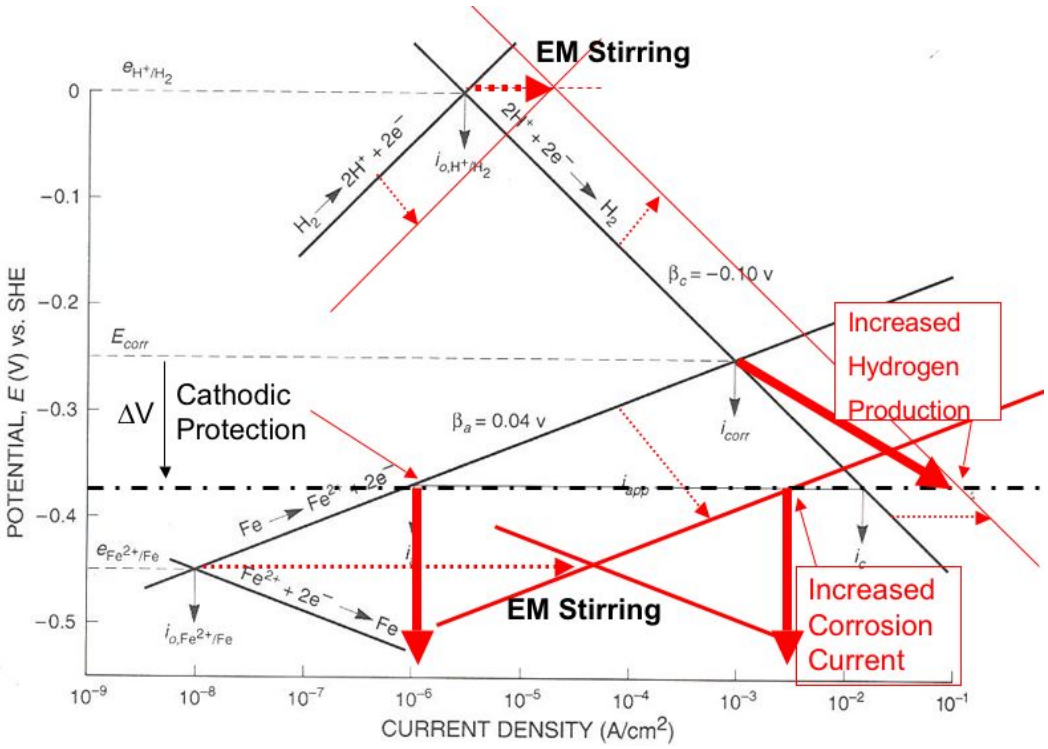

Figure 17. Evans diagram indicating increased hydrogen production and corrosion current due to cathodic protection and Helmholtz-Layer-controlled effects on hydrogen content.

14.0 ELECTROCHEMICAL IMPEDANCE SPECTROSCOPY

Electrochemical impedance spectroscopy (EIS) is a common technique utilized to assess the impedance of an electrode system. Variance of the frequency of the applied AC field allows assessment of a wide variety of chemical and physical properties. Impedance is a function of the resistivity (a measure of the exchange current density), capacitance (a measure of the influence on the HDL), and inductance (a measure of the influence on the GCL).

EIS utilizes a relatively small AC field superimposed on a cathodic or anodic current of choice and is useful for assessment of process dynamics and surface characteristics. The AC voltage variation typically has little or no effect on the phenomena being studied, particularly when a much larger constant applied voltage is being utilized. The potentiodynamic curves for each steel type may be utilized to determine the voltage region in which the working electrode (the specimen) is acting as a cathode.

A consistent testing regime was established and run using CorrWare to coordinate cathodic charging and impedance sweep measurements. A thirty minute cathodic charging step was followed by impedance sweeps at the same voltage, with varied levels of dc voltage, ac voltage, and finally a potentiodynamic polarization sweep.

For the selected steels, the change from anode to cathode occurs between -500 and -550 mV, and therefore the electrochemical impedance analysis was performed at voltages from -550 mV to -1500 mV. The current was set at a minimum of 100 milliamps or 50 milliamps per centimeter squared, whichever value is least. Direct current voltages of -0.55, -0.65, -0.75 V, -0.85 V, -0.95

V, -1.05 V, -1.25 V, and -1.50 V relative to the open circuit potential were applied. In, Figure 18, Figure , and Figure , and Figure 21 electrochemical impedance sweeps at these voltages are given for the frequency range from 0.1 to 100,000 hertz with and without an applied magnetic field of maximum value approximately 0.6 Tesla for X52, X65, X70, and X100 grade pipeline steels, respectively.

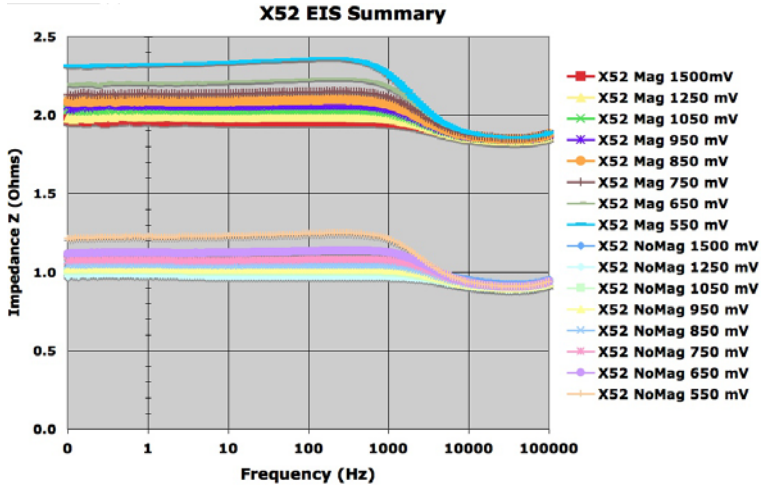

Figure 18 -- Impedance as a function of frequency, measured from 100,000 to 0.1 Hertz, of the 50 mV AC perturbation field for X52 grade steel with varied DC fields applied on the range of -550 to -1500 mV and with approximate magnetic field of 0, 0.6, and 1.0 Tesla.

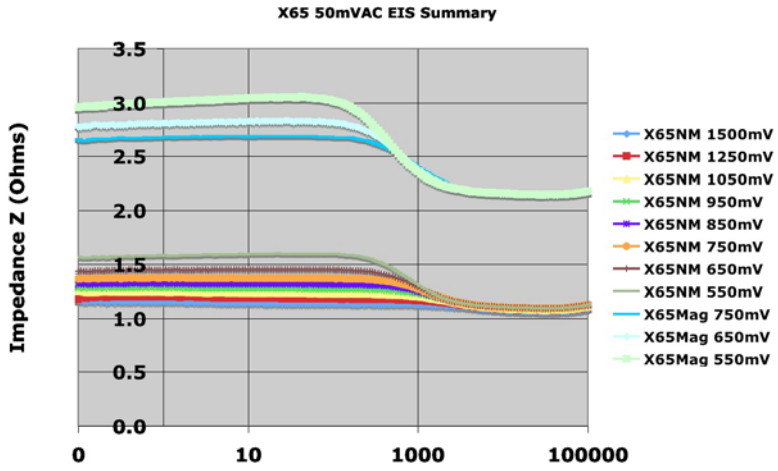

Figure 19 -- Impedance as a function of frequency, measured from 100,000 to 0.1 Hertz, of the 50 mV AC perturbation field for X65 grade steel with varied DC fields applied on the range of -550 to -1500 mV and with approximate magnetic field of 0 (NM), 0.6 (Mag), and 1.0 Tesla.

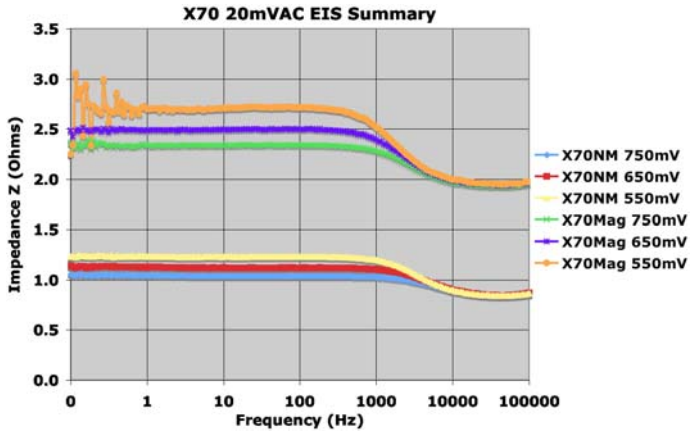

Figure 20 -- Impedance as a function of frequency, measured from 100,000 to 0.1 Hertz, of the 50 mV AC perturbation field for X70 grade steel with varied DC fields applied on the range of -550 to -750 mV.

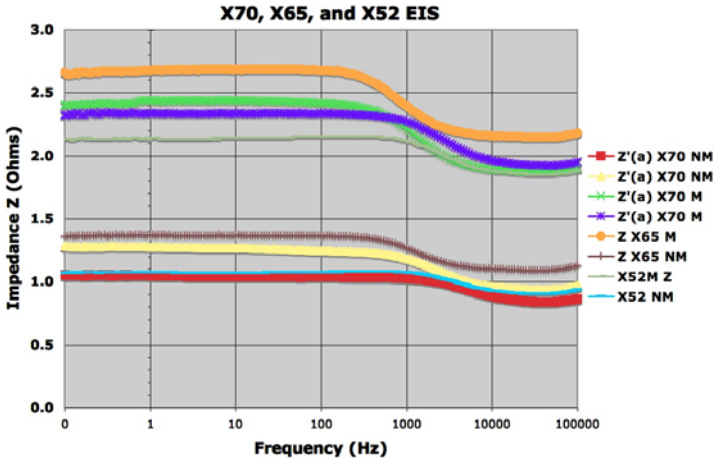

Figure 21 -- Impedance as a function of frequency, measured from 100,000 to 0.1 Hertz, of the 50 mV AC perturbation field for X52, X65, and X70 grade steel with applied DC fields applied on the range of -550 mV

15.0 MAGNETIC PROPERTIES ASSESSMENT

During inline inspection with magnetic tools, a saturating magnetic field is applied and areas of magnetic leakage indicate potential areas of defects. In typical magnetic flux leakage testing, magnetic fields on order of 1.4 to 1.8 Tesla and 3.5 to 20 Oersteds are commonly utilized to ensure complete magnetic saturation. Remanent magnetic fields from 0.3 to 1.5 Teslas are commonly observed to remain in the pipeline steel after a magnetic inspection pig passes, and is dependent upon a number of variables including material composition, stress state, dislocation density, and other factors [Bray and Stanley, 1997].

Magnetic property measurements were made using a Vibrating Sample Magnetometer (VSM) in the preliminary testing [Sanchez, 2005]. For approximate observation of magnetic properties, this technique is sufficient, but for accurate correlation of magnetic properties to observed

magnetocorrosion, improved magnetic properties assessment techniques were utilized. A magnetic hysteresisgraph, in combination with a single-strip tester, was utilized for more accurate measurement of magnetic properties. The arrangement creates a closed magnetic field that minimizes the effect of self-demagnetization, which introduces error into VSM measurements.

Additional VSM measurements of linepipe steel magnetic properties at the National Institute of Standards and Technology (NIST) in Boulder, Colorado for X52 and X70 steels indicated the approximate measured magnetic flux saturation value for both steels to be approximately 1.8 Tesla in the radial (R) direction and 1.6 Tesla in the longitudinal (L) direction. The approximate magnetic remanence determined from VSM hysteresis loops is 1.0 Tesla for X70 steel [Jackson et al, 2006b]. The large measured saturation values are consistent with other CSM-NIST measurements [Sanchez et al, 2005] and values measured from 36 linepipe steels [Nestleroth and Crouch, 1997].

Magnetic hysteresis loops with decreasing maximum applied magnetic field strengths of longitudinal X70 pipeline steel were measured in a single-strip frame in the Metis HYMAC Magnetic Properties Tester and are shown in Figure 22. The single-strip frame is used to create a closed magnetic loop during hysteresis testing, thereby minimizing the uncertainty that arises when accounting for demagnetization of small samples in open magnetic fields, such as in the VSM. The large magnetic saturation for X52 and X70 grade pipeline steels (approximately 1.7 and 1.9 Tesla, respectively) and remanence (approximately 1.2 and 1.28 Tesla, respectively) measured using saturation magnetic fields for X70 are consistent with values measured for 36 pipeline steel specimens [Nestleroth and Crouch, 1997].

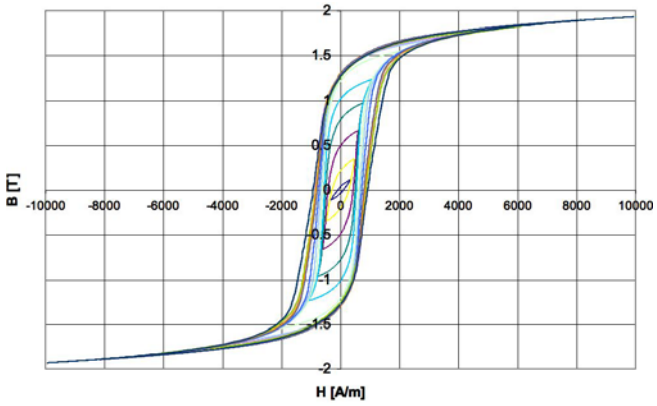

Figure 22 - Magnetic hysteresis loops with varied H_{max} of X70 pipeline steel in single-strip frame

The single-strip frame is used to create a closed magnetic loop during hysteresis testing, thereby eliminating the uncertainty that comes from accounting for demagnetization of small samples in open magnetic fields such as in a vibrating sample magnetometer. The large magnetic saturation (~ 1.9 Tesla) and remanence (~ 1.3 Tesla) measured using saturation magnetic fields are consistent with values measured for 36 pipeline steel specimens [Tiratsoo, 2003]. Figure 23 gives the measured remanent magnetic field as a function of maximum applied field for X70 grade pipeline steel, which is approximately 1.3 Tesla after application of a saturating field and

remains above one Tesla remanence after maximum applied field (H_{max}) of 1,078 A/m (13.55 Oe).

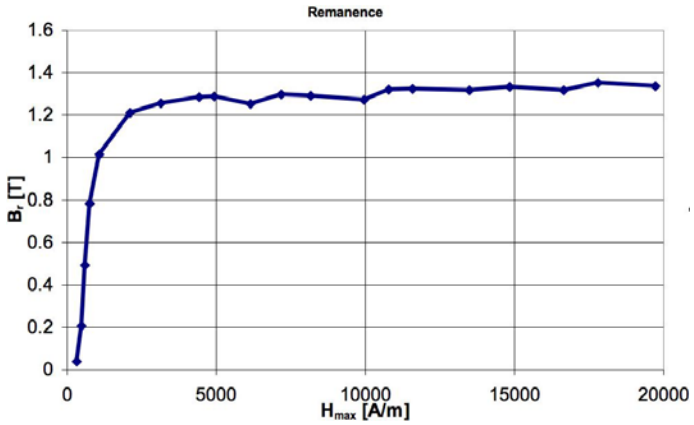

Figure 23 - Magnetic Remanence in X70 pipeline steel as a function of H_{max} in single-strip frame.

Figure 24 indicates the measured magnetic remanence measurements calculated from magnetic hysteresis loops measured at 30 Hertz as a function of maximum applied magnetic field for X70 radial (X70R), X65 longitudinal (X65L), X52 longitudinal and radial samples (X52L and X52R), and longitudinal and radial samples from two X100 type steels (X100A L, X100A R, X100B L, and X100B R). Comparing with the metallography of these samples, it is apparent that the directionality of higher-strength samples results in greater disparity between magnetic properties in the longitudinal and radial directions.

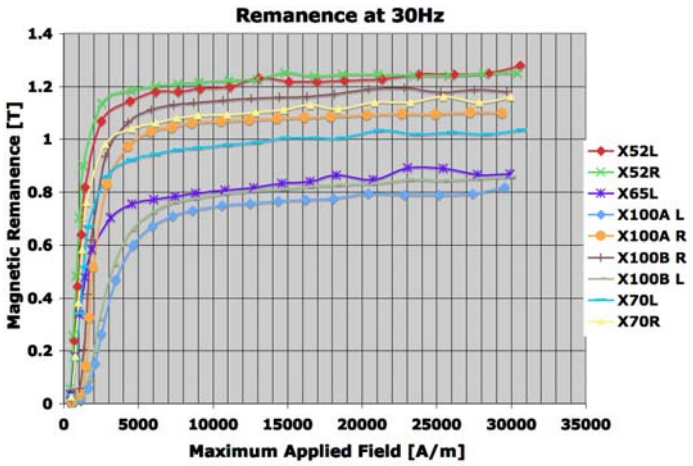

Figure 24 - Magnetic remanence measured at 30 Hertz as a function of maximum applied field.

16.0 PITTING AND CRACKING

In the preliminary research, pitting and cracking measurements were made on X70 and X80 pipeline steels after undergoing electrochemical hydrogen charging for 12, 24, and 36-hour periods with and without applied magnetic fields. A significant increase in pitting and cracking was observed in both steels and the effect increased with time [Sanchez, 2005]. The current

research found similar results with pitting and cracking both substantially increasing in the presence of maximum magnetic fields of 0.6 and 1.0 Tesla, approximately.

Following electrochemical impedance analysis, in combination with cathodic charging at the various levels of DC field using in EIS, the samples were removed for electron microscopy. The results of the pitting and cracking assessment of the current samples is given in Table below.

The accelerated corrosion of the hydrogen charging setup is proposed to be an effective simulation of the effects in a pipeline, in which the sources of hydrogen, electric current, and magnetic field are numerous and corrosion occurs over long periods. Longer-term test with less severe operating parameters and variables should be performed to assess this proposal.

Increased nucleation and propagation of cracks are presumably due to the increased hydrogen level, because the threshold hydrogen level for damage is more easily reached under magnetization. The observed pitting is anodic behavior that suggests magnetization not only increases the cathodic cell reaction, the generation of hydrogen, but also the anodic cell reaction. Table 8 show

Table 8 – Preliminary pitting and cracking Analysis of X52, X65, X70, X80, and X100 type pipeline steels [Sanchez, 2005].

8 Hours	**Pitting**		**Cracking**	
Steel	***Nonmag***	***Magnet***	***Nonmag***	***Magnet***
X52	**No**	**Yes**	**No**	**Yes**
X65	**No**	**Moderate**	**No**	**Moderate**
X70	**Minor**	**Yes**	**No**	**Yes**
X80	**Minor**	**Yes**	**No**	**Yes**
X100	**No**	**Heavy**	**No**	**Heavy**

Table 9 - Pitting and cracking analysis of X52, X65, X70, X80, and X100 type pipeline steels.

8 Hours	**Pitting**	**Pitting**	**Cracking**	**Cracking**
Steel	***Non mag***	***Magnet***	***Non-mag***	***Magnet***
X52	**No**	**Yes**	**No**	**Yes**
X65	**No**	**Moderate**	**No**	**Moderate**
X70	**Minor**	**Yes**	**No**	**Yes**
X80	**Minor**	**Yes**	**No**	**Yes**
X100	**No**	**Heavy**	**No**	**Heavy**

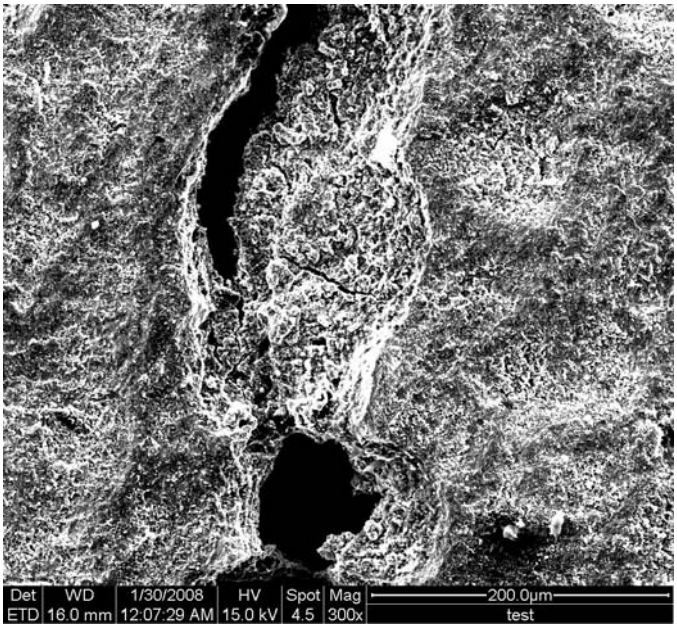

Figure 25 - SEM image of X70 type steel specimen at 300X after charging for eight hours in an approximately 0.6 Tesla magnetic field.

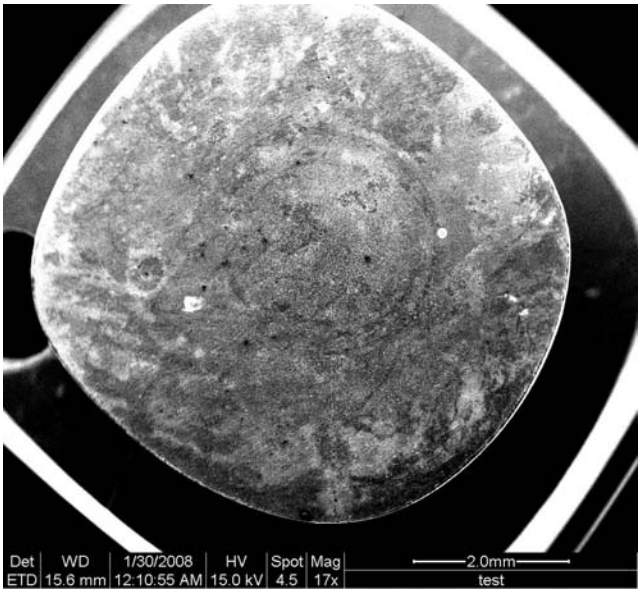

Figure 26 - SEM image of X70 type steel specimen at 31X after charging for eight hours with no Tesla applied magnetic field. Only very minor and sporadic pitting was observed.

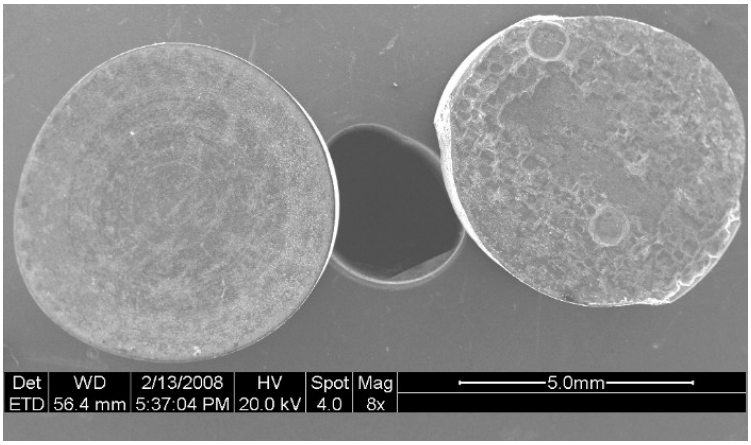

Figure 27 - SEM image of X100 type steel specimen at 8X after charging for eight hours in (left) no magnetic field and (right) an approximately 1.0 Tesla magnetic field.

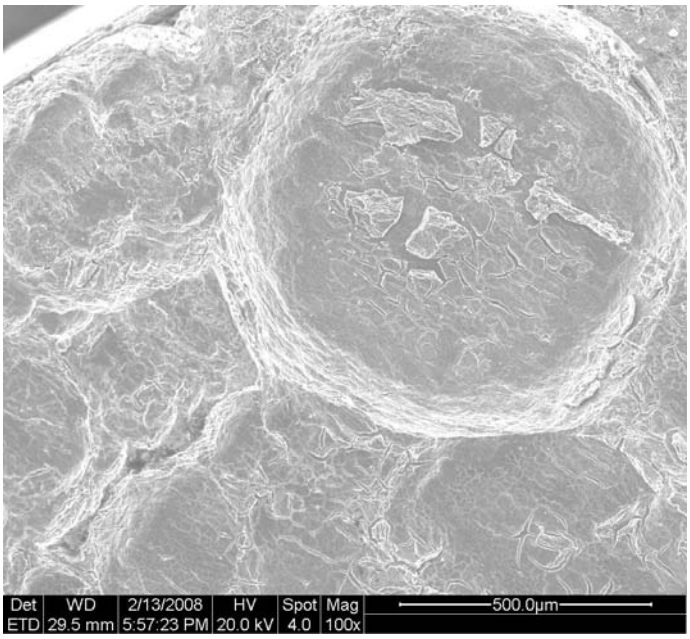

Figure 28 - SEM image of X100 type steel specimen at 100X after charging for eight hours in an approximately 1.0 Tesla magnetic field.

Cathodic hydrogen charging in 0.1 N sulfuric acid solution was performed with voltage held at 50 mV and current density of 500 A/m^2 applied to unmounted steel specimens and specimens mounted between dual one-Tesla permanent magnets for a total field of two Tesla. Cold work also increases the amount of hydrogen content significantly.

Magnetism will cause Lorentz forces to stir the moving ions in the electrolyte passing within a pipeline. Sufficiently high magnetic fields, such as may be remanent after magnetic flux leakage, may create a sufficient Lorentz force to stir the electrolyte and increase the limiting exchange current density. Without any magnetic or electrical fields, corrosion occurs at a rate i_{corr}, where the lines for hydrogen reduction and iron oxidation cross on the Evans diagram. Cathodic protection increases the rate of hydrogen production while decreasing the corrosion current.

Disturbance of the HDL will increase the exchange current and thus shift the polarization curve to greater currents, increasing hydrogen content as well as the corrosion current, as shown in Figure 5. The suggested mechanism based on CSM laboratory data predicts that magnetization-enhanced corrosion damage to the pipeline steel will occur late in the pipeline coating service life. With loss of coating protection, increased cathodic protection return currents through the pipe will increase the Lorentz force (VxB) stirring phenomena if remanent magnetization is present.

17.0 FIELD OBSERVATIONS

A preliminary field assessment was performed for both the hydrogen content assessment and magnetic remanence assessment techniques. This preliminary effort was to help select equipment and practices for consistent field measurements. Pipeline steel (never MFL pigged) in Louisiana was assessed using a laboratory impedance measurement device powered by a portable field power supply and a FW Bell 5070 gaussmeter. It appears that the gaussmeter measurement technique may give acceptable field assessment measurements provided a proper calibration has been performed.

Preliminary in-field hydrogen and magnetic measurements on operating pipelines were performed in Louisiana and Texas; however, the opportunity to assess a major pipeline during and operation downtime was not available. The goal of the trip was to identify pipelines in many different conditions. For hydrogen measurements, any exposed or coated pipeline is necessary. It is very easy to find exposed pipelines, but it is not so easy to find exposed pipelines during smart pigging operations. The laboratory impedance measurement device for hydrogen content assessment (which has been successfully used on small specimens) was insufficient to induce significant currents into thick-walled pipe. This preliminary investigation suggested a much more powerful (higher current) coil arrangement would be necessary. The development of a high-current low-frequency dual-coil impedance analyzer is in progress, in collaboration with other impedance and eddy current equipment developers and experts to achieve the improved sensor capabilities for thick-walled pipe.

New field trials, including a more powerful portable gaussmeter with an improved probe and the modified impedance analyzer, will be performed in January 2008. With successful development of this hydrogen content meter, industrial sites for measurement (particularly those exposed to MFL pigging) will be requested at the JIP joint meeting on January 30-31, 2008.

Magnetic remanence assessment of pipelines during magnetic flux leakage and other smart pigging applications will be measured when a section of an operating pipeline is exposed and undergoing MFL or other smart pigging measurements, during which accurate assessment of magnetic remanence will require contact with the surface of the pipeline. The new axial probe for magnetic assessment should be able to measure the remanence in the pipeline before and after smart pigging. The opportunity to measure the magnetic field during exposed MFL testing is among the current testing goals. Numerous contacts from different companies expressed interest in performing in-field testing for the group.

During the same trip, an invited presentation on “Advanced Non-Destructive Sensors for Materials Characterization” was given at a joint meeting between the Houston chapter of the American Society of Materials and NACE (Corrosion Society). The presentation was an

excellent opportunity to reach out to industry and to try to gain industrial support for the research efforts. Over one hundred people attended the meeting and a number of collaborations and a great deal of interest was established. Meetings with various oil and non-destructive testing companies to discuss future research plans and possible industrial interactions and collaborations yielded promising opportunities

CONCLUSIONS

1. Magnetic fields may cause a significant increase in the corrosion, as indicated by pitting and cracking assessment, and hydrogen content measurements over time.
2. Magnetic properties measurements suggest significant remanence may exist even at relatively low applied magnetic field levels.
3. Thermodynamics calculations based on the various internal and external works involved with magnetic fields suggest that spin magnetization internal work is insufficient to explain the enhanced magnetocorrosion. Magnetostriction and solute-strain models have been described, and a significant contribution to the Helmholtz Free Energy from those terms would be required to explain the enhanced corrosion observed in magnetocorrosion by thermodynamics.
4. Kinetic models, based on electromagnetic stirring in both the metal and the electrolyte, suggest a possible explanation for the enhanced magnetocorrosion behavior.
5. Electrochemical impedance spectroscopy provides a sensitive measurement for assessment of surface corrosion. Magnetic fields cause a significant shift in the measured electrochemical impedance spectroscopy of pipeline steels, which suggests a stirring mechanism may be occurring in both near-electrolyte region (magnetohydrodynamics) and in the metal (Lorentz forces).
6. The magnetohydrodynamic stirring assists in transport of hydrogen to the steel surface.
7. Lorentz forces assist in the transport of hydrogen from the metal surface into the bulk metal, suggesting enhanced hydrogen concentrations based on kinetics.

Acknowledgements

The support and guidance of the U.S. Mineral Management Service, the U.S. Office of Pipeline Safety, and technical discussions with Dr. Ron Goldfarb of the National Institute of Standards and Technology – Magnetic Division are graciously acknowledged.

References

J. E. M. Braid, C.V. Hyatt, D. L. Olson, and G. N. Vigilante, in Hydrogen Management for Welding Applications, pp. 1-282, Proc. Intern. Workshop, October 6-8, 1998, ISBN: 0-662-27989-1, CANMET, Ottawa, Canada (1999).

D.E. Bray, and R.K. Stanley, Nondestructive Evaluation, a Tool in Design, Manufacturing, and Service, Revised Edition, CRC Press, (1997).

J.M.D. Coey, “Magnetoelectrochemistry”, Europhysics News, 34 (6), (2003).

M. Dui, “Elasticity Effects on the Microstructure of Alloys Containing Coherent Precipitates”, in Progress in Materials Science, 40 (2), pp. 79-180, Elsevier Science, Oxford, U.K., (1996).

Y. Fukai, The Metal-Hydrogen System, Springer-Verlag Press, Berlin (1993).

J.E. Jackson, D.L. Olson, A.N. Lasseigne-Jackson, B.Mishra, and T.A. Siewert, “Correlating The Influence of Magnetic Field on Solute Content in Metals Using the Thermodynamic Auxiliary Work Functions”, Proceedings of the Sixteenth Symposium on Thermophysical Properties, July 30- August 4, (2006a), Boulder, CO, USA.

J.E. Jackson, S. Hays, L. Salmans, J.E. Wyatt, “The influence of electric current and magnetic fields on corrosion in steel wire”, CSM Internal Research Report, May, Golden, CO (2006b).

R.A. Jaramillo, S.S. Babu, G.M. Ludtka, R.A. Kisner, J.B. Wilgen, G. Mackiewicz-Ludtka, D.M. Nicholson, S.M. Kelly, M. Murugananth and H.K.D.H. Bhadeshia, “Effect of 30 Tesla Magnetic Field on Transformations in a Novel Bainitic Steel”, Scripta Materialia, 52, pp. 461-466 (2004).

D.A. Jones. *Principles and Prevention of Corrosion*, Prentice-Hall, Inc. Upper Saddle River, NJ (1996).

N.M. Makarov, G.B. Tkachev, V.A. Yarnpol’skijt, and F. Perez Rodriguez, “Current States in a Metal Plate”, J. Phys: Condens. Matter, 5 pp. 7469-7480 (1993).

N.M. Makarov, G.B. Tkachev, V.A. Yarnpol’skijt, L.M. Fisher, and I.F. Voloshin, “Sign-Alternating Current Structure and Oscillations in I-V Characteristics of a Metal Plate”, J. Phys: Condens. Matter, 7 pp. 625-637 (1995).

I. S. Maroef, D. L. Olson, M. Eberhart and G. R. Edwards, “Hydrogen Trapping in Ferritic Steel Weld Metal”, Int. Mat. Rev., vol. 47 (4), pp. 191-223 (2002).

J. McMurray, R.C. Fay., *Chemistry*, 3rd. Edition. Prentice Hall. Upper Saddle River, New Jersey (2001).

J.B. Nestleroth and A.E. Crouch, “Variations of Magnetic Properties in Pipeline Steels”, Prepared for U.S. Dept. of Transportation DTRS56-96-C-0010 Washington, D.C. (1997).

T.R. Ni Mhiochain and J.M.D. Coey, “Numerical simulation of magnetic fields effects on fractal electrodeposits with an adapted diffusion limited aggregation model”, Magnetohydrodynamics 37 pp.169 (2001).

Y.D. Park and D.L. Olson, “The Effect of Hydrogen on Invar Properties”, CSM Internal Research Report, May, Golden, CO (2000).

T.W. Petersen, “Magnetization Changes in Low-Carbon, Ni-Cr-Mo, and High-Strength-Low-Alloy Steels as a Function of Stress”, NISTIR 3962, Electromagnetic Technology Division (September 1991).

F. J. Sanchez, B. Mishra, and D. L. Olson, “Magnetization Effect on Hydrogen Absorption in High-strength Steels and its Implications”, Scripta Mat. 53 (12), pp. 1443-1448 (2005).

F. J. Sanchez, B. Mishra, and D. L. Olson, “An Assessment of Magnetization Effect on Hydrogen Induced Cracking of Pipeline Steels”, submitted to Scripta Mat. 2006.

T. Sohmura and F.E. Fujita, “The effect of Hydrogen on the Magnetic Properties of Fe-Ni Base Invar Alloys”, J. Phys. F: Met. Phys. 10, 743-755, (1980).

M. Stern and A.C. Makrides, “Electrode Assembly for Electrochemical Measurements”, *J. Electrochemical Society* **107**, p.782 (1960).

J. Tiratsoo, Ed., Pipeline Pigging and Integrity Technology, 656 pgs., Scientific Surveys, Ltd., Beaconsfield, UK, and Clarion Technical Publishers, Houston, TX, (2003).